High-performance polarization-independent beam splitters and MZI in silicon carbide integrated platforms for single-photon manipulation

Xiaodong Shi, Yaoqin Lu, Nianhua Peng, Karsten Rottwitt, Haiyan Ou

***Abstract*—Silicon carbide (SiC), having various intrinsic color centers, is a highly promising optical materials for making monolithic quantum integrated photonic circuits, by combining the single-photon sources with the integrated photonic components in SiC integrated platforms. Based on this quantum-material platform, we propose polarization-independent 1 $\times$ 2 and 2 $\times$ 2 multimode interference based beam splitters and Mach-Zehnder interferometers (MZI) for single-photon manipulation with unknown polarization states. We experimentally demonstrate that these devices exhibit excellent performances with incident light at both high power (>-10 dBm) and ultra-low power (<-100 dBm). The 1 $\times$ 2 and 2 $\times$ 2 beam splitters have low average loss of 1 dB and 1.5 dB, with a wide bandwidth of >100 nm and >70 nm, respectively. The MZI exhibits high transmittance, with a visibility of 98.3% and 97.6% for the high-power measurement and an even higher visibility of 99.0 $\pm$ 0.4% and 98.7 $\pm$ 0.6% for the ultra-low power measurement, for the TE and TM polarizations, respectively.**

***Index Terms*—Integrated photonics, silicon carbide, beam splitting, interferometer.**

I. Introduction

Silicon carbide (SiC) is a traditional material, that has been extensively used in power electronics and mechanics, thanks to the excellent electronic, mechanic, thermal and chemical properties, such as high breakdown field, large Young's modulus, high thermal conductivity, and high chemical inertness, making the devices work stably under extreme environments with a long lifetime and benefiting sustainable development [1], [2]. During the last decade, SiC has entered into integrated photonics, thanks to its beneficial optical properties of low material loss, relatively high refractive index, and wide transparent window. Compared to silicon, which is most widely used in integrated photonics, SiC, as a wide-bandgap semiconductor with both strong second- and third-order optical nonlinearities, does not suffer from two-photon absorption and subsequent free-carrier absorption in the telecom wavelength band, making this material suitable for high-power nonlinear applications [3], [4], [5], [6], [7]. These superior optical properties of SiC allow a variety of on-chip optical applications, for example, efficient wavelength conversion, frequency comb generation, thermo-optic modulation, and electro-optic modulation [8], [9], [10], [11]. SiC-on-insulator (SiCOI) stacks enabling tight light confinement have emerged to make high-refractive-index-contrast waveguides, which takes the advantage of complementary metal–oxide–semiconductor (CMOS) compatible waveguide fabrication processes [12], [13]. Several passive devices have been proposed in SiC integrated platforms, such as microrings, microdisks, photonic crystals, polarization beam splitters, and gratings, making possible multiple functionalities integrated together in a single chip [7], [14], [15], [16].

Meanwhile, SiC is also regarded as an excellent quantum material, which possesses many different kinds of intrinsic color centers, including silicon vacancy, divacancy, and nitrogen vacancy [17], [18]. Chromium, vanadium, and molybdenum can also be doped in SiC to generate electron spins [19], [20], [21]. The color centers, which are optically addressable, can also be created by different methods, for example, direct laser writing, ion implantation, and thermal annealing [22], [23], [24], and are able to be isolated for being single-photon sources [18]. Hence, the states of the electrons or emitted photons can be prepared as qubits [25]. Compared with the other deterministic single-photon sources based on quantum dots, the color center based single-photon sources, embedded inside the material, are more stable, easily fabricated and integrated with planar photonic components [26], [27]. Especially, telecom-wavelength SiC single-photon sources have been observed, which is compatible with the current optical communication networks, benefiting quantum communications, such as quantum key distribution (QKD) [20], [21], [28]. As a result, SiC holds a remarkable promise for monolithic quantum photonic integrated circuits, by combining the SiC color center based single-photon sources with the SiC integrated platforms [29].

The beam splitter, splitting the photon flow into two traces, is a fundamental component for most of the quantum measurements, and is widely used in quantum photonics. For example, the purity of the SiC single-photon sources has been measured by the coincidence between the signals from two traces after the 50%:50% beam splitter via the Hanbury-Brown and Twiss (HBT) measurement, in a free-space setup [30]. Mach-Zehnder interferometer (MZI) based modulators are also composed of beam splitters. Utilizing the thermo-optic or electro-optic effects of SiC, efficient phase modulation can be achieved. With the MZI, a superposition of bunching state and antibunching of a pair of entangled photons can be acquired.[31]. Additionally,

X. Shi, Y. Lu, K. Rottwitt and H. Ou are with DTU Fotonik, Technical University of Denmark, DK-2800 Lyngby, Denmark. (email: xshi@fotonik.dtu.dk, yaolu@dtu.dk, karo@fotonik.dtu.dk, haou@fotonik.dtu.dk)

N. Peng is with Ion Beam Centre, University of Surry, Guildford, GU2 7XH, UK. (email: n.peng@surrey.ac.uk)

Corresponding author: Haiyan Ou

This work is supported by European Union's Horizon 2020 Future and Emerging Technologies Open (SiComb, No.899679) and European Union's Horizon 2020 Research and Innovation (RADIATE, No.824096).

Hong-Ou-Mandel (HOM) experiments, requiring two-photon interference, also utilize the MZI, from which the information of the purity and the indistinguishability of the single-photon source can be obtained [32]. Thus, high-performance on-chip beam splitters and MZI are very essential for single-photon manipulation and SiC quantum integrated circuits. However, so far, there is a lack of design and demonstration on beam splitters or MZI in SiC integrated platforms.

A high-performance beam splitter exhibits low loss, broad operational bandwidth, and polarization independence, simultaneously. Many different types of beam splitters have been studied on silicon platforms, for example, Y junctions, directional couplers, adiabatic couplers, as well as multimode interferometers (MMI) [33], [34], [35]. Among these types, MMI does not only enable low loss and broad bandwidth, but also allows variable-ratio power splitting and multiple mode splitting for flexible multimode signal processing [36], [37], [38]. Meanwhile, MMI-based on-chip quantum interferometers have been mostly investigated with low loss, wide bandwidth, high visibility, and high fabrication tolerance, compared to directional couplers or Y junctions [39], [40], [41], [42], [43]. Especially for quantum applications, polarization independence is a key feature. The single photons generated from different defects may have different polarization states, determined by the defect emission dipole orientation [30]. When applying spontaneous parametric down conversion to obtain photon pairs from SiC, Type II second nonlinear processes, containing co-polarized photons, may occur [44]. In addition, polarization-independent MZI is also able to reduce the bias of the two arms, so that it benefits the high-dimensional QKD, involving the polarization as one of the degrees of freedom. Thus, the polarization-independent MMI-based beam splitter and MZI in SiC integrated platforms are much worthy exploring.

In this paper, we propose high-performance polarization-independent 1 × 2 and 2 × 2 MMI based beam splitters and MZI in 4H-SiCOI integrated platforms, working in both high-power and ultra-low power regimes. The simulated 1 × 2 and 2 × 2 MMI have low loss of <1 dB for both polarizations, over 280 nm wavelength range from 1360 nm to 1640 nm and over 70 nm wavelength range from 1510 nm to 1580 nm, respectively. The experimental results show that the polarization-independent MZI exhibits high visibility of 98.3% and 97.6% in the high-power regime, and of 99.0 ± 0.4% and 98.7 ± 0.6% in the ultra-low power regime, for TE and TM polarizations, respectively.

II. Design and Simulation

We design and simulate polarization-independent 1 × 2 and 2 × 2 MMI based beam splitters and MZI based on the finite-difference time-domain (FDTD) method, of which the schematics are shown in Fig.1.

A. Self-image principle

The MMI-based beam splitters rely on the self-image mechanism, that the input optical field is reproduced in a single or multiple-fold images periodically along the propagation direction [45]. The design of the 50%:50% 1 × 2 and 2 × 2 MMI based beam splitters is based on the symmetric interference and the general interference principles, respectively.

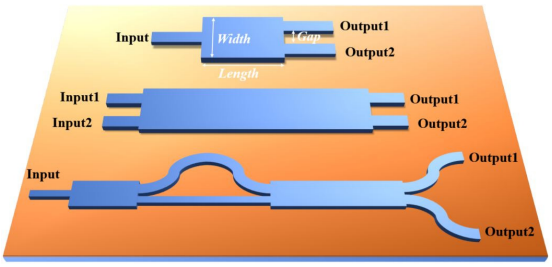

Fig. 1. Schematic of the 1 × 2 MMI, 2 × 2 MMI, and MZI.

The beat length of the MMI is calculated by

$$L_\pi = \frac{\pi}{\beta_0 - \beta_1}, \tag{1}$$

where β_0 and β_1 are the propagation constants of the fundamental and the first-order modes, respectively. The propagation constant is given by

$$\beta = \frac{2\pi n_{\text{eff}}}{\lambda}, \tag{2}$$

where n_{eff} is the effective refractive index of the mode, and λ is the wavelength. In order to make the polarization-independent MMI, the beat length of the TE and TM polarization should be equivalent as

$$L_{\pi,\text{TE}} = L_{\pi,\text{TM}}, \tag{3}$$

indicating that the effective refractive index difference between the fundamental mode and the first-order mode of the TE and TM polarizations should have minimal difference, simultaneously.

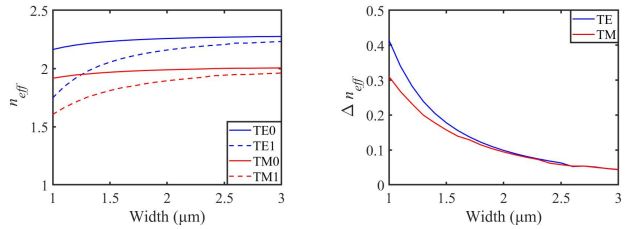

Fig. 2. (a) Effective refractive index of the fundamental and first-order modes and (b) effective refractive index difference between the fundamental mode and the first-order mode, as a function of the waveguide width, for both polarizations.

We simulate the effective refractive index at 1550 nm of the fundamental and first-order modes of both polarizations as a function of the SiC waveguide width, with a fixed waveguide height of 400 nm, which has been typically used for thermo-optic effect measurement, optical bistability, efficient four-wave mixing, optical parametric oscillation, and polarization beam splitting [7], [10], [16]. As seen in Fig.2(a), the effective refractive index of the fundamental modes is larger than

that of the corresponding first-order mode, but the effective refractive index of the first-order mode increases faster with the increasing waveguide width for both polarizations. Then, we analyze the effective refractive index difference between the fundamental mode and the first-order mode of both polarizations as a function of the waveguide width, seen in Fig.2(b). The effective refractive index difference of both modes decreases with the increasing waveguide width, and becomes overlapping from the width of 2.0 μm, making possible polarization-insensitive multimode interference. Thus, considering the compact integration of the photonic devices, we select the width of 2.0 μm, as the starting parameter for the following optimization of both 1 × 2 and 2 × 2 MMI.

The beat length of both modes can be calculated to be approximately 8.0 μm, according to Eq.1. For the 1 × 2 MMI with the input waveguide connecting to the center of the MMI and the 2 × 2 MMI, the length with the two-fold image can be calculated through

$$L_{1\times2} = \frac{3L_\pi}{8}, \tag{4}$$

and

$$L_{2\times2} = \frac{3L_\pi}{2}, \tag{5}$$

which are 3 μm and 12 μm, respectively. These calculated values are used as a reference in the following optimization.

B. 1 × 2 MMI

We optimize three parameters in the 1 × 2 MMI at 1550 nm, including the gap between the two output waveguides, the MMI length and the MMI width. The input and the output waveguides have a width of 600 nm, which only support the fundamental TE and TM modes, with an effective refractive index of 1.90 and 1.78, respectively.

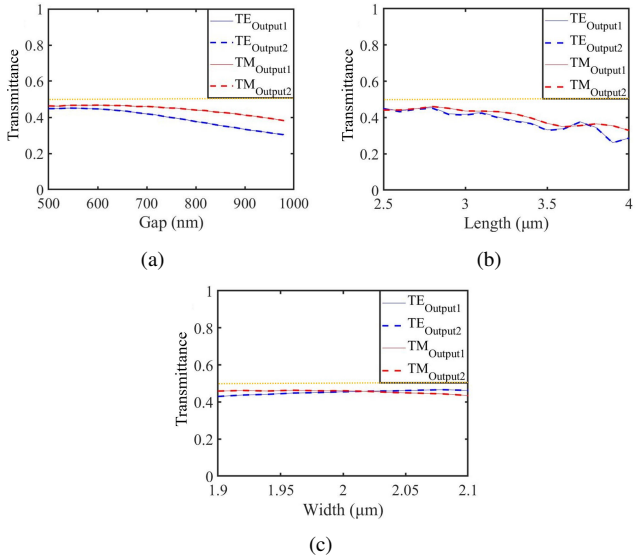

Fig. 3. 1 × 2 MMI transmittance as a function of (a) the gap between the two output waveguides, (b) the length, and (c) the width. The yellow dash line shows the ideal output efficiency of 50%.

The transmittance versus the gap is plotted in Fig.3(a), with fixed 1 × 2 MMI length and width of 3.0 μm and 2.0 μm, respectively. It is noticed that the transmittance of both polarizations at Output1 and Output2 are almost equivalent, because of the symmetry. The transmittance of the TE and TM polarized light increases a little at first and then decreases with the increasing gap, from 500 nm to 1000 nm. A narrower gap can result in a problem of undesirable light coupling after the interference, due to the close distance between the two output waveguides. With the gap of 530 nm, the transmission of TE and TM polarized light has a very high efficiency of 45% and 47%, respectively. Within the gap range from 500 nm to 700 nm, both TE and TM polarized light has a high transmittance of >40%, equivalent to a loss of <1 dB, given by $IL = -10\log_{10}\frac{2T_{\text{Output}}}{T_{\text{Input}}}$. The transmittance versus the 1 × 2 MMI length is plotted in Fig.3(b). With the length of 2.8 μm, the transmission of TE and TM polarized light has a very high efficiency of 46% and 47%, respectively. The optimized MMI length is approximately equal to the calculated value in the theoretical analysis. Within the MMI length range from 2.5 μm to 3.2 μm, both TE and TM polarized light has a high transmittance of >40%, corresponding to a low loss of <1 dB. The transmittance versus the MMI width is plotted in Fig.3(c). With the width of 2.02 μm, the transmission of TE and TM polarized light has the same high efficiency of 47%, showing the polarization-insensitive property of the 1 × 2 MMI. Within the MMI width range from 1.9 μm to 2.1 μm, both TE and TM polarized light has a high transmittance of >43%, corresponding a low loss of <0.65 dB. During the optimization, it can be found that all the parameters have very wide bandwidths (>200 nm), that enable high transmittance, indicating that the device can have high fabrication tolerance.

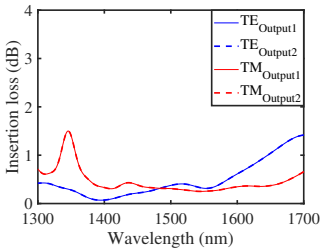

Fig. 4. The insertion loss of the 1 × 2 MMI with the optimized parameters as a function of the wavelength.

Using the optimized parameters, we simulate the insertion loss of the 1 × 2 MMI for both polarizations from 1300 nm to 1700 nm, shown in Fig.4. The well overlapping transmittance of Output1 and Output2 for both polarizations is observed, indicating effectively equivalent beam splitting. A wide operational bandwidth can be observed, that both polarizations have a low loss of <1 dB, within the wavelength range from 1360 nm to 1640 nm. The transmittance efficiency of the TE and TM polarizations has <0.2 dB difference from 1430 nm to 1590 nm, indicating efficient and broadband polarization-independent beam splitting.

C. 2 × 2 MMI

We optimize three parameters in the 2 × 2 MMI at 1550 nm, including the gap between the two input and output

waveguides, the MMI length and the MMI width. Since the 2 × 2 MMI length is four times as long as the 1 × 2 MMI length, in terms of Eq.4 and 5, we use the 2 × 2 MMI length of 11.2 μm, as the starting parameter for the optimization. The input and the output waveguides have the same dimension as those in the 1 × 2 MMI, which is 600 nm.

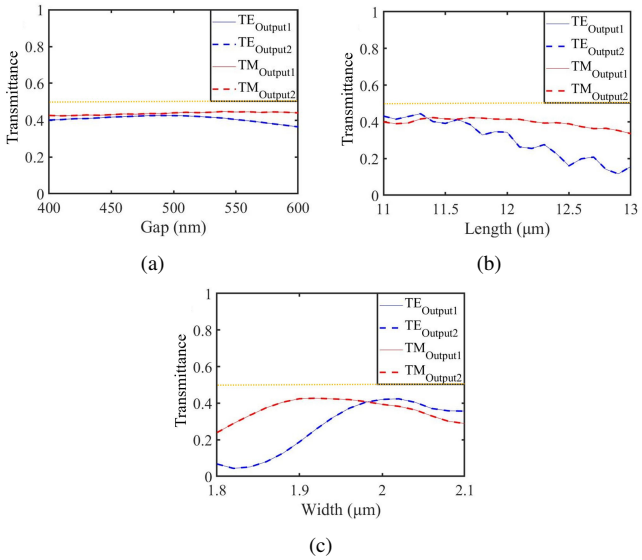

Fig. 5. 2 × 2 MMI transmittance as a function of (a) the gap between the two input and output waveguides, (b) the length, and (c) the width. The yellow dash line shows the ideal output efficiency of 50%.

The transmittance versus the gap is plotted in Fig.5(a). Within the gap range from 430 nm to 510 nm, both polarizations have 50%:50% beam splitting with a low loss of <1 dB and a power difference of <5%. Polarization independence appears at a gap of 490 nm, with a high transmittance of 42%. The transmittance versus the 2 × 2 MMI length is plotted in Fig.5(b). Within the MMI length range from 11 μm to 11.7 μm, both TE and TM polarizations have a low loss of <1 dB. The optimized length for polarization independence is 11.4 μm, with a high transmittance of 43%. The transmittance versus the MMI width is plotted in Fig.5(c). With a width of 1.97 μm, the transmission of TE and TM polarized light has the same high transmittance of 43%.

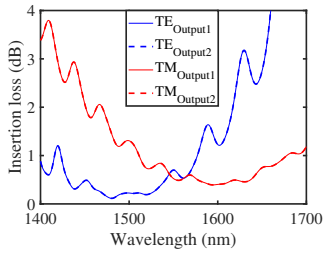

Fig. 6. The insertion loss of the 2 × 2 MMI with the optimized parameters as a function of the wavelength.

Using the optimized parameters, we plot the insertion loss in Fig.6. The well overlapping transmittance of Output1 and Output2 for both polarizations is also observed, indicating that the equivalent beam splitting is effective. At around 1560 nm, the transmittance of the TE and TM polarizations are almost equivalent with a low loss of <1 dB, showing efficient polarization-independent beam splitting. To enhance the polarization independence and increase the transmittance, one could apply subwavelength metastructures incorporated in the MMI and tailor the connection part between the single-mode waveguide and the MMI with a taper for further improvement, respectively [46].

D. MZI

The MZI can be made by combining a 1 × 2 MMI with a 2 × 2 MMI, which have been optimized above. The energy distribution of the TE and TM polarizations in the MZI with equal interferometric arm length is shown in Fig.7(a) and Fig.7(b), respectively. It is seen that the light is injected from the input of the 1 × 2 MMI, equally split into two interferometric arms with the same length, coupled into the 2 × 2 MMI, and equally coupled out from the two outputs.

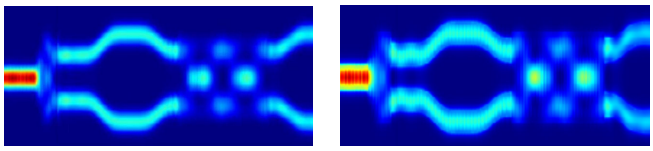

Fig. 7. Energy distribution of (a) TE and (b) TM polarized light propagating along the proposed MZI.

The transmittance of the MZI as a function of the phase shift of both polarizations are plot in Fig.8. The phase shift is achieved by varying the refractive index of one arm in the simulation. The maximum transmittance of the TE and TM polarization is 79% and 82%, respectively, which indicates the polarization independence. The visibility of the MZI, reflecting the contrast of interference, is expressed as

$$V = \frac{P_{max} - P_{min}}{P_{max} + P_{min}}, \tag{6}$$

where P_{max} and P_{min} are the maximum and the minimum power at Output1 or Output2, respectively. According to Eq.6, we find that the TE and TM polarizations have high-visibility interference in the proposed MZI, which are calculated as 99.0% and 97.8%, respectively.

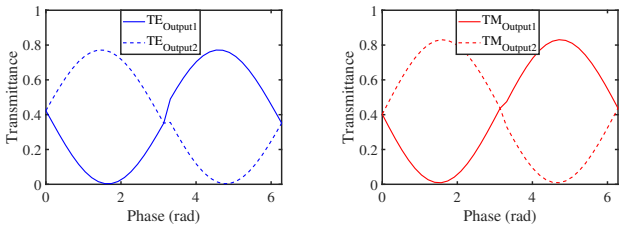

Fig. 8. Simulated MZI transmittance as a function of the phase shift of (a) TE and (b) TM polarizations.

III. Fabrication and Characterization

After the simulation of the 1 × 2 and 2 × 2 beam splitters and the MZI, we fabricate the devices in the 4H-SiCOI integrated platform [16].

The 4H-SiCOI chip is prepared by the ion-cut process. First, H_2^+ species are implanted into a 4H-SiC wafer to form a damaged layer underneath the 4H-SiC surface. Second, a silicon wafer is thermally oxidized to form a SiO_2 layer. Third, the two wafers are bonded together with hydrophilic bonding through a reverse RCA process, followed by a high temperature annealing at 700° for 3 hours to enhance the bonding strength. Fourth, the bonded wafers are annealed at 850° to exfoliate the thin 4H-SiC film from the 4H-SiC wafer, and the 4H-SiCOI stack is obtained. Finally, the 4H-SiC thin film is thermally oxidized to reduce the thickness down to 400 nm.

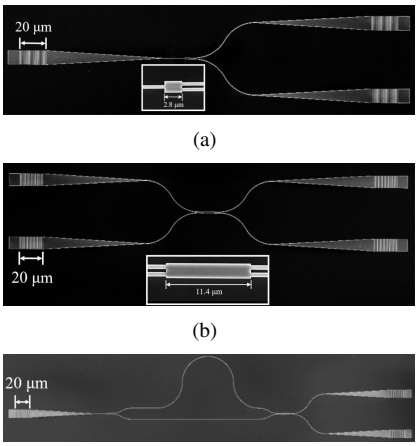

Fig. 9. SEM images of the fabricated (a) 1 × 2, (b) 2 × 2 MMI, and (c) unbalanced MZI. The insets in (a) and (b) show the zoom-in images of the 1 × 2 and 2 × 2 MMI in the center of the testing device.

For the device fabrication in the 4H-SiCOI chip, first, the pattern is defined on the e-beam resist, by e-beam lithography. Second, the pattern is transferred on a metal mask by e-beam evaporation of aluminum and a following lift-off process. Third, the device is fabricated on the 4H-SiC layer by inductively coupled plasma reactive ion etching. Scanning electron microscope (SEM) images of the fabricated devices are shown in Fig.9. The input and output ports of the beam splitters and the MZI are connected to the identical polarization-insensitive grating couplers for the device testing [7].

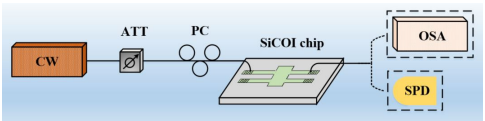

Fig. 10. A schematic of the experimental setup.

The schematic of the experimental setup to test the devices is shown in Fig.10. A tunable continuous-wave (CW) laser (ANDO AQ4321D) is used as the light source. A tunable attenuator (ATT) is used to attenuate the power to quantum level for the ultra-low power measurement. A polarization controller (PC) is used to modulate the polarization of the light beam to quasi-TE or quasi-TM mode. The light is coupled between the optical fiber and the waveguide through a pair of polarization-insensitive grating couplers [7]. For the high-power performance characterization, the transmittance is measured by an optical spectrum analyzer (OSA) (ANDO AQ6317B), which is synchronized with the tunable CW laser. For the ultra-low-power performance characterization, the photons are counted by the single-photon detector (SPD) (ID Quantique ID230).

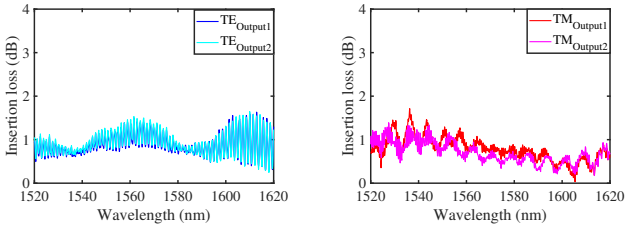

Fig. 11. Measured insertion loss of (a) TE and (b) TM polarized light, transmitting through the fabricated 1 × 2 MMI, as a function of the wavelength.

It is noticed that the insertion loss of the 1 × 2 and 2 × 2 MMI and the transmittance of the MZI show the high-power performance of the device itself, after the subtraction of the transmittance of the grating couplers. The characterization results of the 1 × 2 MMI are shown in Fig.11. The measured transmittance of both polarizations at two output ports is almost the same, indicating equivalent beam splitting. The transmittance is generally flat for both polarizations, from 1520 nm to 1620 nm. The average loss of the device is about 1 dB generally for both polarizations within the 100 nm measurement range, which means that the 1 × 2 MMI works effectively and efficiently with strong polarization independence, and has ultra-wide operational bandwidth, at least covering the C and L telecom optical wavelength bands. The ripples shown in the experimental results are considered to be induced by the multimode interference.

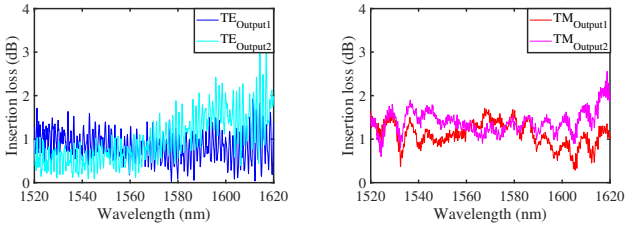

Fig. 12. Measured insertion loss of (a) TE and (b) TM polarized light, transmitting through the fabricated 2 × 2 MMI, as a function of the wavelength.

The characterization results of the 2 × 2 MMI are shown in Fig.12. At around 1570 nm, the 2 × 2 MMI enables equivalent beam splitting for both polarizations. The average loss is about 0.8 dB and 1.2 dB for the TE and TM polarizations, respectively, indicating efficient polarization-independent beam

splitting. Within the 100 nm measurement range, the loss is below 2 dB.

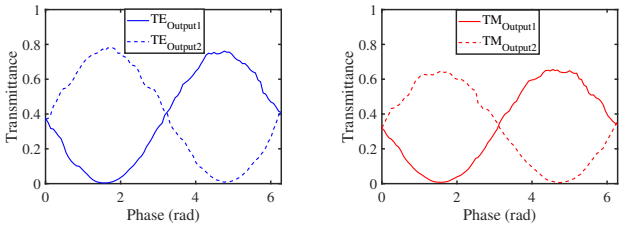

Fig. 13. Measured MZI transmittance as a function of the phase shift of (a) TE and (b) TM polarizations.

The characterization results of the MZI with unequal interferometric arm length for TE and TM polarizations are shown in Fig.13. The power at the two outputs depends on the the phase difference between the two arms, given by $\Delta\phi = 2\pi n_{\text{eff}}\Delta L/\lambda$, where ΔL is the delay length, which is about 91.3 μm in this experiment. The 2π phase difference in the measurement is achieved by sweeping the wavelength with 13.9 nm and 14.8 nm at around 1550 nm, for TE and TM polarizations, respectively. The maximum transmittance of the MZI is 78% and 66%, for TE and TM polarizations, respectively. According to Eq.6, the visibility of TE and TM polarizations is calculated as high as 98.3% and 97.6%, respectively, confirming the high visibility of the MZI at high power.

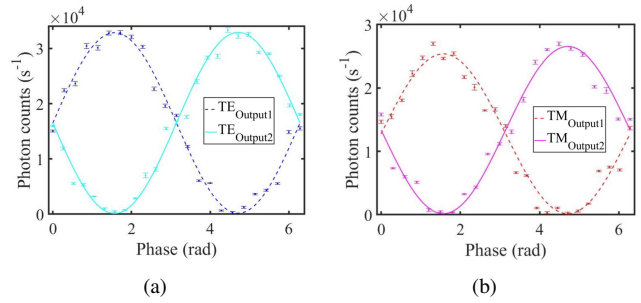

Fig. 14. Measured photon counts as a function of the phase shift of (a) TE and (b) TM polarizations in the MZI.

We then suppress the input power down to <-100 dBm to evaluate the performance at the ultra-low power, as probabilistic events occurs when the power reaches the quantum level. The photon counts for both polarizations are detected by the single-photon detector. Figure 14 shows the measured data and the fitted sine curves of the nonclassical characterization of the MZI. It shows that the photon counts are almost equivalent at two outputs with a π shift for both polarizations. The visibility of the MZI at ultra-low power can be expressed by

$$V' = \frac{C_{max} - C_{min}}{C_{max} + C_{min}}, \tag{7}$$

where $C_{max/min}$ denotes the maximum/minimum photon counts, through replacing the optical power by the photon counts in Eq.6 [40], [41]. The visibility of the MZI for the TE and TM polarizations is calculated as high as 99.0 ± 0.4% and 98.7 ± 0.6%, respectively, confirming the high performance of the polarization-independent MZI at ultra-low power. The classical interference pattern of the MZI can reflect its quantum interference pattern [47], [48]. Thus, it is fair to infer that these devices can also perform well in the quantum regime.

IV. Discussion

The proposed MZI shows very high visibility at both high power and ultra-low power. The visibility at ultra-low power is slightly higher than that at high power for both polarizations from the experimental results. For the ultra-low power measurement, photons transmit through the device and arrive at the detector for counting. If some photons are absorbed or scattered randomly, it is not possible to detect and count. Compared to the high-power measurement, the ultra-low power measurement is more sensitive to the loss and the random processes, which could induce lower detected photon counts at the destructive interference, and thus results in higher visibility.

When integrating color centers in SiC as the single-photon sources to the demonstrated MZI, more measurements can be conducted. For example, HOM experiments, measuring the photon interference through MZI, are able to characterize the purity (single-photon state property) and indistinguishability (one photon's property in relation to another photon's) of the single-photon sources [49]. The visibility of HOM interference is given by

$$V_{HOM} = \frac{C_{max} - C_{min}}{C_{max}}. \tag{8}$$

It can be predicted that, for ideal single-photon sources, the visibility can be as high as 99.5% and 99.4% for TE and TM polarized photons with the fabricated MZI, respectively, based on the above quantum measurement results. For the indistinguishability measurement of photon pairs, two photons having the maximal overlap with the quantum states are highly indistinguishable. With an interference pattern expressed as $C = \frac{1}{2}(1 - I(\Delta t))$, where Δt denotes the time delay, and I denotes the indistinguishability, the visibility of the HOM equals the indistinguishability, $V_{HOM} = I(\Delta t = 0)$. For the purity measurement of single photons generated from a single-photon source with different time bins, the visibility of the HOM interference is equivalent to the purity of the single-photon source, when the temporal delay between the two photons is 0, given by $V_{HOM} = P(\Delta t = 0)$.

Theoretically, the visibility of the single-photon source is related to the trace of the squared mixed-state density matrix, following by

$$V_{HOM} = Tr(\rho_1\rho_2) = \frac{P_1(\rho_1) + P_2(\rho_2) - O(\rho_1, \rho_2)}{2}, \tag{9}$$

where ρ is the state of a photon, and O is the overlap between two states [50]. For an ideal entangled photon pair, having $P_1(\rho_1) = P_2(\rho_2) = 0$, the visibility only shows the overlap between two states, which is related to the indistinguishability. For two ideal indistinguishable photons, having $O(\rho_1, \rho_2) = 0$, the visibility reflects the purity of the state. Ideally, these

measurements requires lossless 50%:50% beam splitting after interference. High-performance beam splitters and MZI, demonstrated in this work, are able to keep and maintain high fidelity of the single-photon states, when preparing and manipulating single photons in the SiC integrated platforms.

The time delay or the phase change in the MZI can be potentially achieved by utilizing the thermo-optic effect or the electro-optic effect in SiC. Recently, the thermo-optic coefficient of 4H-SiCOI has been reported to be 4.21×10^{-5} K^{-1} [10]. Hence, it is possible to make thermo-optic MZI modulators with on-chip integrated heaters in the 4H-SiCOI integrated platform. The thermo-optic effect induces the effective refractive index change of the waveguide, resulting in a phase shift, given by $\Delta\varphi = 2\pi\frac{\Delta n_{\text{eff}} L_i}{\lambda}$, where L_i is the interaction length of one arm that is thermally modulated. Assuming the 4H-SiC MZI has an interaction length of 1 mm on one arm, in order to have a $\frac{\pi}{2}$ phase shift at 1550 nm, the temperature of the interaction 4H-SiC waveguide is supposed to change by 9.2 K.

V. Conclusion

In this paper, we numerically and experimentally demonstrate polarization-independent 1×2 and 2×2 MMI-based beam splitters and MZI in the 4H-SiCOI integrated platform, working at both high power and ultra-low power. The 1×2 and 2×2 beam splitters exhibit low average loss of 1 dB and 1.5 dB, with wide bandwidth of >100 nm and >70 nm, respectively, for both polarizations, which shows strong polarization insensitivity. Composed of the beam splitters, the MZI exhibits very high high-power visibility of 98.3% and 97.6% and ultra-low-power visibility of $99.0 \pm 0.4\%$ and $98.7 \pm 0.4\%$, for TE and TM polarizations, respectively. The experimental results indicate that these high-performance SiC photonic components can be applied for both classical optical signal processing and single-photon manipulation especially for the SiC single-photon sources with unknown polarization states. Meanwhile, it is an important step forward to reveal the potential of the SiC integrated platform as monolithically integrated quantum optical circuits.

Acknowledgment

Xiaodong Shi and Yaoqin Lu would like to thank Jingjing Zhang, Yueguang Zhou and Weichen Fan for useful discussions.

References

[1] C. Eddy and D. Gaskill, "Silicon carbide as a platform for power electronics," *Science*, vol. 324, no. 5933, pp. 1398–1400, 2009.

[2] G. Krotz, W. Legner, C. Wapner, H. Moller, H. Sonntag, and G. Muller, "Silicon carbide as a mechanical material," in *Proceedings of the International Solid-State Sensors and Actuators Conference-TRANSDUCERS'95*, vol. 2. IEEE, 1995, pp. 186–189.

[3] X. Shi, K. Guo, J. B. Christensen, M. A. U. Castaneda, X. Liu, H. Ou, and K. Rottwitt, "Multichannel photon-pair generation with strong and uniform spectral correlation in a silicon microring resonator," *Physical Review Applied*, vol. 12, no. 3, p. 034053, 2019.

[4] K. Guo, X. Shi, X. Wang, J. Yang, Y. Ding, H. Ou, and Y. Zhao, "Generation rate scaling: the quality factor optimization of microring resonators for photon-pair sources," *Photonics Research*, vol. 6, no. 6, pp. 587–596, Jun 2018.

[5] K. Guo, L. Yang, X. Shi, X. Liu, Y. Cao, J. Zhang, X. Wang, J. Yang, H. Ou, and Y. Zhao, "Nonclassical optical bistability and resonance-locked regime of photon-pair sources using silicon microring resonator," *Physical Review Applied*, vol. 11, no. 3, p. 034007, 2019.

[6] D. M. Lukin, C. Dory, M. A. Guidry, K. Y. Yang, S. D. Mishra, R. Trivedi, M. Radulaski, S. Sun, D. Vercruysse, G. H. Ahn *et al.*, "4h-silicon-carbide-on-insulator for integrated quantum and nonlinear photonics," *Nature Photonics*, vol. 14, no. 5, pp. 330–334, 2020.

[7] X. Shi, W. Fan, Y. Lu, A. K. Hansen, M. Chi, A. Yi, X. Ou, K. Rottwitt, and H. Ou, "Polarization and spatial mode dependent four-wave mixing in a 4h-silicon carbide microring resonator," *APL Photonics*, vol. 6, no. 7, p. 076106, 2021.

[8] M. A. Guidry, K. Y. Yang, D. M. Lukin, A. Markosyan, J. Yang, M. M. Fejer, and J. Vučković, "Optical parametric oscillation in silicon carbide nanophotonics," *Optica*, vol. 7, no. 9, pp. 1139–1142, 2020.

[9] X. Wu, T. Fan, A. A. Eftekhar, and A. Adibi, "High-q microresonators integrated with microheaters on a 3c-sic-on-insulator platform," *Optics Letters*, vol. 44, no. 20, pp. 4941–4944, 2019.

[10] X. Shi, W. Fan, A. K. Hansen, M. Chi, A. Yi, X. Ou, K. Rottwitt, and H. Ou, "Thermal behaviors and optical parametric oscillation in 4h-silicon carbide integrated platforms," *Advanced Photonics Research*, vol. 2, no. 10, p. 2100068, 2021.

[11] T. Fan, X. Wu, S. R. Vangapandu, A. H. Hosseinnia, A. A. Eftekhar, and A. Adibi, "Racetrack microresonator based electro-optic phase shifters on a 3c silicon-carbide-on-insulator platform," *Optics Letters*, vol. 46, no. 9, pp. 2135–2138, 2021.

[12] P. Xing, D. Ma, K. J. Ooi, J. W. Choi, A. M. Agarwal, and D. Tan, "Cmos-compatible pecvd silicon carbide platform for linear and nonlinear optics," *ACS Photonics*, vol. 6, no. 5, pp. 1162–1167, 2019.

[13] D. M. Lukin, M. A. Guidry, and J. Vučković, "Integrated quantum photonics with silicon carbide: challenges and prospects," *PRX Quantum*, vol. 1, no. 2, p. 020102, 2020.

[14] X. Lu, J. Y. Lee, P. X.-L. Feng, and Q. Lin, "High q silicon carbide microdisk resonator," *Applied Physics Letters*, vol. 104, no. 18, p. 181103, 2014.

[15] B.-S. Song, T. Asano, S. Jeon, H. Kim, C. Chen, D. D. Kang, and S. Noda, "Ultrahigh-q photonic crystal nanocavities based on 4h silicon carbide," *Optica*, vol. 6, no. 8, pp. 991–995, 2019.

[16] X. Shi, J. Zhang, W. Fan, Y. Lu, N. Peng, K. Rottwitt, and H. Ou, "Compact low-birefringence polarization beam splitter using vertical-dual-slot waveguides in silicon carbide integrated platforms," *Photonics Research*, vol. 10, no. 1, pp. A8–A13, 2022.

[17] S. Castelletto, B. C. Johnson, and A. Boretti, "Quantum effects in silicon carbide hold promise for novel integrated devices and sensors," *Advanced Optical Materials*, vol. 1, no. 9, pp. 609–625, 2013.

[18] A. Lohrmann, B. Johnson, J. McCallum, and S. Castelletto, "A review on single photon sources in silicon carbide," *Reports on Progress in Physics*, vol. 80, no. 3, p. 034502, 2017.

[19] B. Diler, S. J. Whiteley, C. P. Anderson, G. Wolfowicz, M. E. Wesson, E. S. Bielejec, F. J. Heremans, and D. D. Awschalom, "Coherent control and high-fidelity readout of chromium ions in commercial silicon carbide," *npj Quantum Information*, vol. 6, no. 1, pp. 1–6, 2020.

[20] J. Schneider, H. Müller, K. Maier, W. Wilkening, F. Fuchs, A. Dörnen, S. Leibenzeder, and R. Stein, "Infrared spectra and electron spin resonance of vanadium deep level impurities in silicon carbide," *Applied Physics Letters*, vol. 56, no. 12, pp. 1184–1186, 1990.

[21] T. Bosma, G. J. Lof, C. M. Gilardoni, O. V. Zwier, F. Hendriks, B. Magnusson, A. Ellison, A. Gällström, I. G. Ivanov, N. Son *et al.*, "Identification and tunable optical coherent control of transition-metal spins in silicon carbide," *npj Quantum Information*, vol. 4, no. 1, pp. 1–7, 2018.

[22] S. Castelletto, A. F. M. Almutairi, K. Kumagai, T. Katkus, Y. Hayasaki, B. Johnson, and S. Juodkazis, "Photoluminescence in hexagonal silicon carbide by direct femtosecond laser writing," *Optics Letters*, vol. 43, no. 24, pp. 6077–6080, 2018.

[23] M. Widmann, M. Niethammer, T. Makino, T. Rendler, S. Lasse, T. Ohshima, J. Ul Hassan, N. Tien Son, S.-Y. Lee, and J. Wrachtrup, "Bright single photon sources in lateral silicon carbide light emitting diodes," *Applied Physics Letters*, vol. 112, no. 23, p. 231103, 2018.

[24] M. Rühl, C. Ott, S. Götzinger, M. Krieger, and H. Weber, "Controlled generation of intrinsic near-infrared color centers in 4h-sic via proton irradiation and annealing," *Applied Physics Letters*, vol. 113, no. 12, p. 122102, 2018.

[25] D. Riedel, F. Fuchs, H. Kraus, S. Väth, A. Sperlich, V. Dyakonov, A. Soltamova, P. Baranov, V. Ilyin, and G. Astakhov, "Resonant addressing and manipulation of silicon vacancy qubits in silicon carbide," *Physical Review Letters*, vol. 109, no. 22, p. 226402, 2012.

[26] G. Calusine, A. Politi, and D. D. Awschalom, "Silicon carbide photonic crystal cavities with integrated color centers," *Applied Physics Letters*, vol. 105, no. 1, p. 011123, 2014.

[27] D. O. Bracher, X. Zhang, and E. L. Hu, "Selective purcell enhancement of two closely linked zero-phonon transitions of a silicon carbide color center," *Proceedings of the National Academy of Sciences*, vol. 114, no. 16, pp. 4060–4065, 2017.

[28] S. A. Zargaleh, S. Hameau, B. Eble, F. Margaillan, H. J. von Bardeleben, J.-L. Cantin, and W. Gao, "Nitrogen vacancy center in cubic silicon carbide: A promising qubit in the 1.5 μ m spectral range for photonic quantum networks," *Physical Review B*, vol. 98, no. 16, p. 165203, 2018.

[29] S. Castelletto, A. Peruzzo, C. Bonato, B. C. Johnson, M. Radulaski, H. Ou, F. Kaiser, and J. Wrachtrup, "Silicon carbide photonics bridging quantum technology," *ACS Photonics*, 2022.

[30] A. Lohrmann, N. Iwamoto, Z. Bodrog, S. Castelletto, T. Ohshima, T. Karle, A. Gali, S. Prawer, J. McCallum, and B. Johnson, "Single-photon emitting diode in silicon carbide," *Nature Communications*, vol. 6, no. 1, pp. 1–7, 2015.

[31] J. Wang, F. Sciarrino, A. Laing, and M. G. Thompson, "Integrated photonic quantum technologies," *Nature Photonics*, vol. 14, no. 5, pp. 273–284, 2020.

[32] J. C. Adcock, J. Bao, Y. Chi, X. Chen, D. Bacco, Q. Gong, L. K. Oxenløwe, J. Wang, and Y. Ding, "Advances in silicon quantum photonics," *IEEE Journal of Selected Topics in Quantum Electronics*, vol. 27, no. 2, pp. 1–24, 2020.

[33] L. Han, B. P.-P. Kuo, N. Alic, and S. Radic, "Ultra-broadband multimode 3db optical power splitter using an adiabatic coupler and a y-branch," *Optics Express*, vol. 26, no. 11, pp. 14 800–14 809, 2018.

[34] Y. Luo, Y. Yu, M. Ye, C. Sun, and X. Zhang, "Integrated dual-mode 3 db power coupler based on tapered directional coupler," *Scientific Reports*, vol. 6, no. 1, pp. 1–7, 2016.

[35] H. Yun, W. Shi, Y. Wang, L. Chrostowski, and N. A. Jaeger, "2x2 adiabatic 3-db coupler on silicon-on-insulator rib waveguides," in *Photonics North 2013*, vol. 8915. International Society for Optics and Photonics, 2013, p. 89150V.

[36] N. S. Lagali, M. R. Paiam, R. I. MacDonald, A. Driessen *et al.*, "Analysis of generalized mach-zehnder interferometers for variable-ratio power splitting and optimized switching," *Journal of Lightwave Technology*, vol. 17, no. 12, p. 2542, 1999.

[37] J. Leuthold and C. H. Joyner, "Multimode interference couplers with tunable power splitting ratios," *Journal of Lightwave Technology*, vol. 19, no. 5, p. 700, 2001.

[38] J. S. Yu, S. M. Choi, and Y. T. Lee, "Design and fabrication of a 1$\times$ n ingaasp/inp mmi power splitter with a weakly guided ridge waveguide structure," *Journal of the Korean Physical Society*, vol. 36, no. 2, pp. 84–89, 2000.

[39] D. Bonneau, E. Engin, K. Ohira, N. Suzuki, H. Yoshida, N. Iizuka, M. Ezaki, C. M. Natarajan, M. G. Tanner, R. H. Hadfield *et al.*, "Quantum interference and manipulation of entanglement in silicon wire waveguide quantum circuits," *New Journal of Physics*, vol. 14, no. 4, p. 045003, 2012.

[40] J. Zhang, K. Guo, M. Gao, Y. Gao, and J. Yang, "Design of polarization-insensitive high-visibility silicon-on-insulator quantum interferometer," *Scientific Reports*, vol. 8, no. 1, pp. 1–7, 2018.

[41] J. Zhang, K. Guo, J. Yang, H. Huang, Y. Li, M. Gao, S. Fu, and Y. Gao, "Toward a realizable design of an on-chip optically driven quantum interferometer at telecommunication wavelengths," *Physical Review Applied*, vol. 10, no. 5, p. 054029, 2018.

[42] S. F. Preble, M. L. Fanto, J. A. Steidle, C. C. Tison, G. A. Howland, Z. Wang, and P. M. Alsing, "On-chip quantum interference from a single silicon ring-resonator source," *Physical Review Applied*, vol. 4, no. 2, p. 021001, 2015.

[43] A. Prokhodtsov, V. Kovalyuk, P. An, A. Golikov, R. Shakhovoy, V. Sharoglazova, A. Udaltsov, Y. Kurochkin, and G. Goltsman, "Silicon nitride mach-zehnder interferometer for on-chip quantum random number generation," in *Journal of Physics: Conference Series*, vol. 1695, no. 1. IOP Publishing, 2020, p. 012118.

[44] P. Lundquist, W. Lin, G. Wong, M. Razeghi, and J. Ketterson, "Second harmonic generation in hexagonal silicon carbide," *Applied Physics Letters*, vol. 66, no. 15, pp. 1883–1885, 1995.

[45] L. B. Soldano and E. C. Pennings, "Optical multi-mode interference devices based on self-imaging: principles and applications," *Journal of Lightwave Technology*, vol. 13, no. 4, pp. 615–627, 1995.

[46] W. Zhong and J. Xiao, "Ultracompact polarization-insensitive power splitter using subwavelength-grating-based mmi couplers on an soi platform," *Applied Optics*, vol. 59, no. 7, pp. 1991–1997, 2020.

[47] N. Ramírez-Cruz, M. Bastarrachea-Magnani, and V. Velázquez, "Quantum anatomy of the classical interference of n-photon states in a mach-zehnder interferometer," in *Journal of Physics: Conference Series*, vol. 698, no. 1. IOP Publishing, 2016, p. 012015.

[48] J. Zhang, Z. Zhang, C. Ma, X. Chen, L. Liu, W. Zhao, X. Song, H. Zhang, Y. Yu, H. Chen, and J. Yang, "Ultra-compact and ultra-broadband polarization-insensitive mach–zehnder interferometer in silicon-on-insulator platform for quantum internet application," *Photonics*, vol. 8, no. 10, 2021.

[49] C. Osorio, N. Sangouard, and R. T. Thew, "On the purity and indistinguishability of down-converted photons," *Journal of Physics B: Atomic, Molecular and Optical Physics*, vol. 46, no. 5, p. 055501, 2013.

[50] P. J. Mosley, J. S. Lundeen, B. J. Smith, and I. A. Walmsley, "Conditional preparation of single photons using parametric downconversion: a recipe for purity," *New Journal of Physics*, vol. 10, no. 9, p. 093011, 2008.